www.acsnano.org

Stabilizing Lattice Oxygen via Interfacial B—O Complexing for a 4.6 V LiCoO₂ Cathode

Jimin Qiu,[#] Yuchen Ji,*^{,#} Wenfang Li, Yuhang Li, Wenguang Zhao, Yunxing Zuo, Weiyuan Huang, Chen Zhu, Mingjian Zhang, Guorui Zheng, Luyi Yang, Feng Pan,* and Zu-Wei Yin*



Downloaded via UNIV TOWN OF SHENZHEN on November 18, 2025 at 07:11:32 (UTC). See https://pubs.acs.org/sharingguidelines for options on how to legitimately share published articles.

Cite This: ACS Nano 2025, 19, 34306-34317



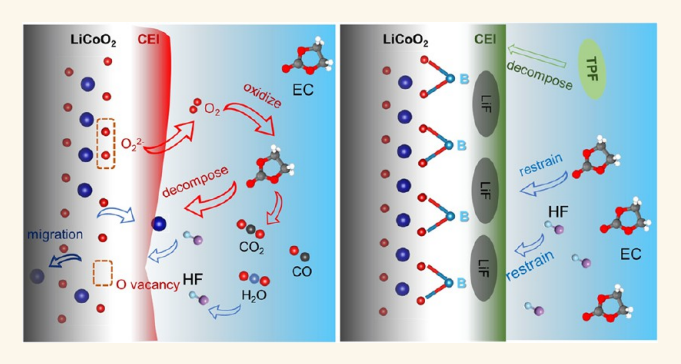
ACCESS I

III Metrics & More

Article Recommendations

s Supporting Information

ABSTRACT: Lithium cobalt oxide (LiCoO₂) cathodes suffer serious structure instability when charged to high voltage (>4.5 V), including H1-3 phase transition, cobalt dissolution, and interfacial side reactions, which are closely related to the instability of surface lattice oxygen. Herein, an interfacial B–O complexing strategy was proposed to stabilize the surface lattice oxygen of LiCoO₂ at 4.6 V, through the preferential coordination between derived products of the tris-(pentafluorophenyl)borane electrolyte additive and LiCoO₂. Combining a series of in situ and ex situ characterization methods with temporal and spatial resolution, it was revealed that the emergence of peroxy-like species (O_2^{2-}) at high



potentials is one of the origins of the instability of $LiCoO_2$, which can be well inhibited thanks to interfacial B-O complexing. Thus, oxygen loss and interfacial side reactions can be drastically retarded, which consequently provides a more stable chemical environment for Co element, avoiding the dissolution and valence reduction of Co. Owing to the well-anchored Co and O elements, undesirable phase transition and local coordination structure change are suppressed, hence improving the capacity retention and rate performance of $LiCoO_2$ at 4.6 V. This study provides an interfacial complexing strategy to stabilize the high-voltage $LiCoO_2$ cathode.

KEYWORDS: Li-ion batteries, high-voltage LiCoO2, surface lattice oxygen, interfacial B-O complexing, electrolyte modification

1. INTRODUCTION

Owing to the advantages of high theoretical capacity (274 mAh g⁻¹), high energy density, high rate performance, and good air stability, lithium cobalt oxide (LiCoO₂, abbreviated as "LCO") has served as a successful battery cathode material for Li-ion batteries, especially in consumer electronic devices. ^{1–5} To fulfill the ever-increasing performance requirements for higher specific capacity and energy density, expanding the working voltage range of LCO is necessary. 6-9 Theoretically, the capacity of LCO can be raised to 220 mAh g⁻¹ when the cutoff voltage increases to 4.6 V, offering additional >60% specific energy.^{8,10} However, the detrimental structural and interfacial issues triggered from high-voltage operations, including continuous electrolyte decomposition, gas releases, and the irreversible phase transition from a layered phase to spinel-like and rock-salt phases, result in the capacity decay during cycling and hinder the realization of high-voltage LCO in practical use. 6-8,11 Such structural and interfacial issues are closely related to the instability of lattice oxygen. 12-17

In layered oxide cathode materials, lattice oxygen participating in charge compensation (O-redox) often occurs at high voltages. ¹⁸ For LCO, when the delithiation amount of

 ${\rm Li_{1-x}CoO_2}$ is above 0.5 (x>0.5), further extraction of Li ions requires the oxidation of ${\rm O^{2-}}$ for charge compensation, 19,20 which may become a significant origin of LCO interfacial instability and failure at high voltages. It has been reported that various products are formed during the O-redox reactions of high-voltage LCO, including ${\rm O^{n-}},^{21}$ peroxy-like compounds (O–O dimer), 13 oxygen free radicals (${\rm O^{\bullet}}$), 22 and ${\rm O_2},^{23}$ which are highly oxidative toward carbonate-based electrolytes, forming a thick cathode—electrolyte interphase (CEI) layer on the surface of LCO. $^{23-25}$ In addition, the generation of oxygen free radicals and ${\rm O_2}$ also forms oxygen vacancies in LCO, 26 resulting in the migration of Co atoms and the formation of spinel and rock-salt phases. 27

Received: July 16, 2025
Revised: September 8, 2025
Accepted: September 9, 2025
Published: September 16, 2025





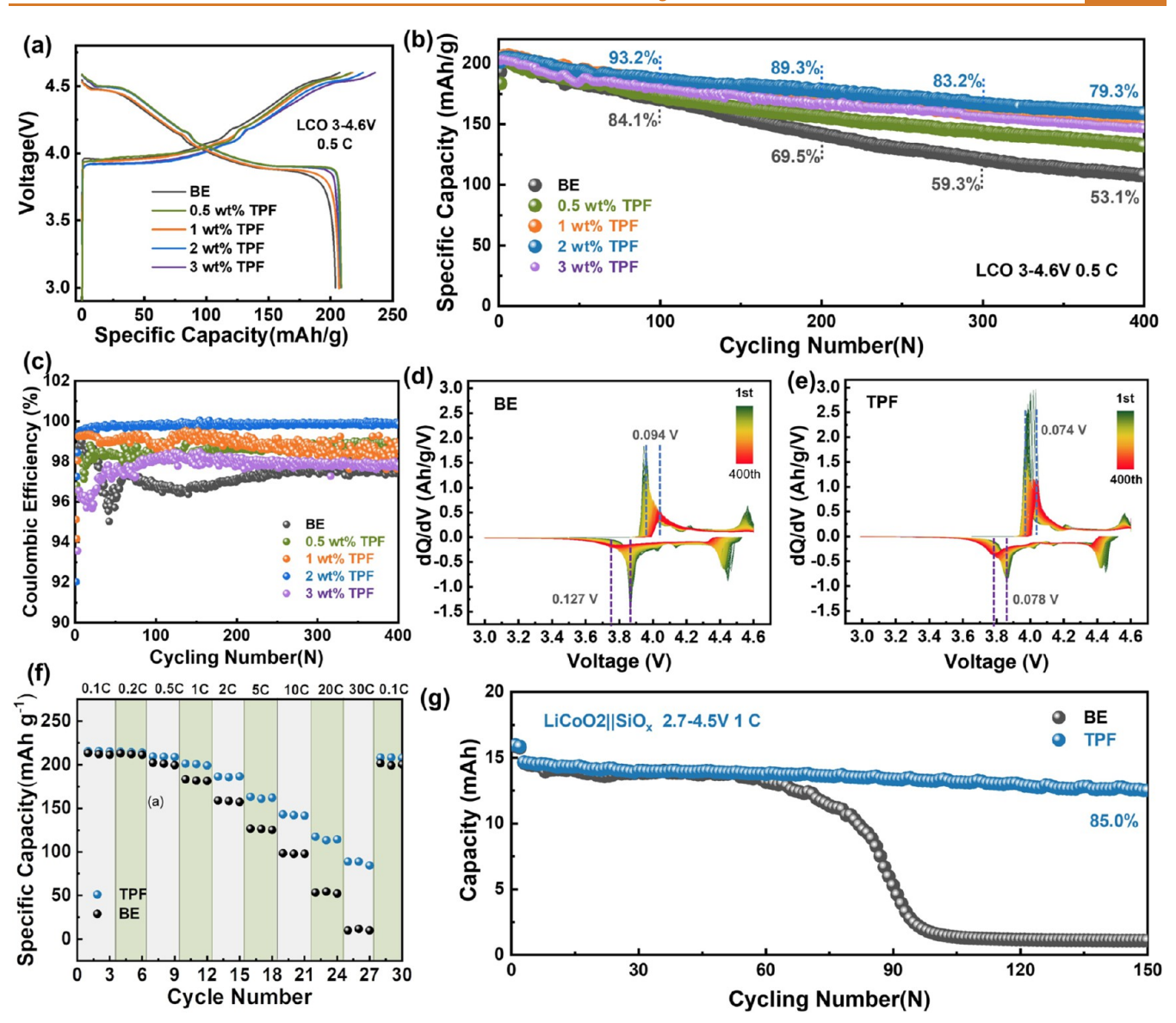


Figure 1. Electrochemical performance of the LCO cathode using various electrolytes. (a) Charge—discharge profiles of LillLCO half-cells in various electrolytes at the first cycle within 3–4.6 V. (b) Cyclic performance of LillLCO half-cells in various electrolytes. (c) Coulombic efficiency of LillLCO half-cells in various electrolytes during the long cycling process. (d, e) dQ/dV curves for 400 cycles in the 3–4.6 V voltage range of LillLCO half-cells using BE (d) and TPF-BE (e). (f) Rate performances of LillLCO half-cells using BE and TPF-BE. (g) Cyclic performance of SiO_x||LCO pouch cells using BE and TPF-BE at a voltage range of 2.7–4.5 V and a current density of 1C (1C = 200 mA g⁻¹).

Some methods have been proved as effective ways to stabilize lattice oxygen and mitigate oxygen release, such as bulk doping, 6,8,28 surface coating, 9,25,29,30 electrolyte engineering, etc. 4 Bulk ion doping (i.e., Al³+, Mg²+, and Ti⁴+) can regulate the electronic structure of LCO, while the surface coatings (i.e., carbon, spinel) mainly play a protective role in preventing the side reactions between LCO and the electrolyte. Electrolyte engineering similarly protects the LCO cathode material through cathode—electrolyte interphase (CEI) formation, 4 but a lack of in-depth mechanism studies of electrolyte regulation affects the lattice oxygen stability.

Herein, an interfacial B–O complexing approach to stabilize the lattice oxygen of LCO at 4.6 V was proposed via introducing the tris(pentafluorophenyl)borane additive into the electrolyte. By combining theoretical calculations with various in situ and ex situ characterization methods, it was

revealed that the electron-withdrawing boron atoms could complex with surficial lattice oxygen atoms and reduce the projected density of states (PDOS) of oxygen. Owing to B–O complexing, the formation of peroxy-like species $({\rm O_2}^{2-})$ and subsequent lattice oxygen loss have been significantly inhibited at high voltages. The stabilized lattice oxygen also contributes to suppressing Co dissolution and Co valence reduction. With the enhanced stability of both lattice oxygen and Co in LCO, an undesirable phase transition occurs at the surface, and its migration to the bulk can be mitigated. Consequently, the cycling stability and rate performance of LCO at 4.6 V can be drastically improved.

2. RESULTS/DISCUSSION

2.1. Electrochemical Performance of 4.6 V LCO. In this study, a conventional carbonate electrolyte was chosen as the

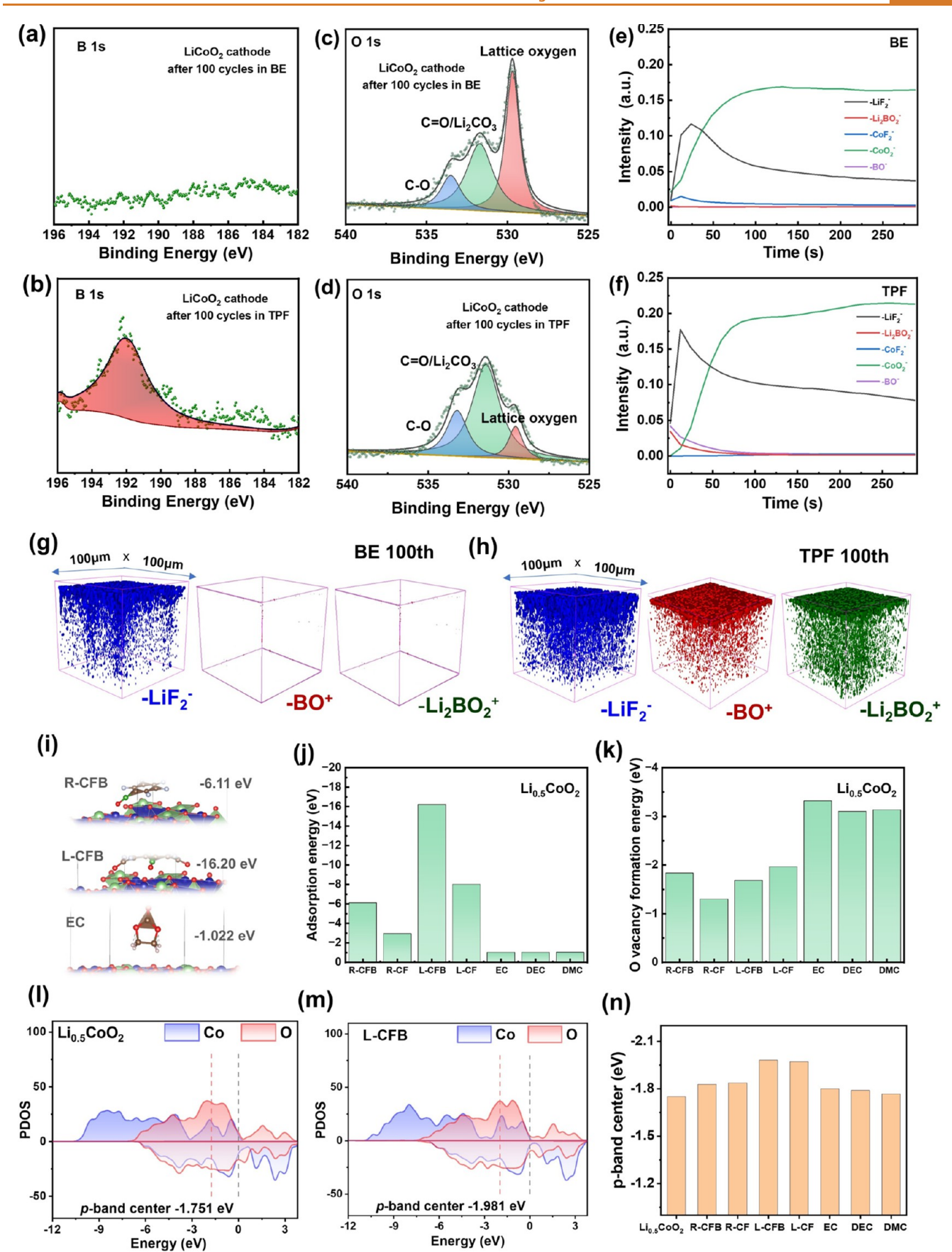


Figure 2. Characterizations and theory calculations of the B-O complexation interface. B 1s XPS spectra of LCO after 100 cycles in BE (a) and TPF-BE (b). O 1s XPS spectra of LCO after 100 cycles in BE (c) and TPF-BE (d). Time-of-flight secondary ion mass spectrometry (TOF-SIMS) signal intensities of various components at the LCO surface as etching in (e) and (f). 3D distribution of various components

Figure 2. continued

inner CEI layers measured via TOF-SIMS in BE (g) and TPF-BE (h). (i) Adsorption structure of the decomposed TPF additive and ethylene carbonate (EC) on $\text{Li}_{0.5}\text{CoO}_2$. Adsorption energy (j) and oxygen vacancy formation energy (k) of various components of the electrolyte on $\text{Li}_{0.5}\text{CoO}_2$. Projected density of states (PDOS) of oxygen and Co atoms in $\text{Li}_{0.5}\text{CoO}_2$ (l) and adsorbed with a linear structural C-F product with a B atom (m). (n) Summarized calculated projected density of states (PDOS) of oxygen atoms in $\text{Li}_{0.5}\text{CoO}_2$ under different adsorption configurations.

base electrolyte (abbreviated as BE) and tris-(pentafluorophenyl)borane (abbreviated as TPF) was employed as the additive. The corresponding molecular structures of various main components are presented in Figure S1. Both the Raman and Fourier transform infrared (FT-IR) spectra of electrolytes (Figures S2 and S3) remain the same after the introduction of TPF, indicating that the solvation structure of the electrolyte is not influenced by the additive. Thus, it is rational to speculate that the effect of TPF on the electrochemistry can be attributed to the interfacial reconstruction on the surface of LCO.

The improvement effect of the TPF additive on the electrochemical performance of the LCO cathode was verified by assembling LillLiCoO2 half-cells and electrolytes with various TPF contents of 0.5, 1, 2, and 3 wt %, which were compared with BE to screen out the optimal ratio. As the charge and discharge curves are presented in Figure 1a, it is noteworthy that the introduction of the TPF additive slightly increases the initial discharge specific capacity. With the increase of TPF contents, the specific capacity of the first-cycle charging gradually increases (Table S1), which can be ascribed to the oxidative decomposition reaction of the TPF additive during the charging process. As presented in Figure 1b, the battery in BE retained only 53.1% of the initial discharge capacity after 400 long cycles at 0.5C, while the capacity retention of the batteries in the electrolyte systems containing 0.5, 1, 2, and 3 wt % TPF additive increased to 64.2, 73.6, 79.3 and 72.8%, respectively. The difference in the Coulombic efficiencies of the five electrolytes during 400 cycles (Figure 1c) demonstrates that compared with BE, the Coulombic efficiency can also be improved by the TPF additive. Among different ratios, it is clear that the electrolyte with 2 wt % TPF additive exhibits both the highest capacity retention and the highest long-term average Coulombic efficiency. Therefore, it was chosen as the optimal electrolyte composition for the subsequent electrochemical and characterization tests (abbreviated as TPF-BE in the following text).

The evolution of the corresponding dQ/dV curves of BE and TPF-BE during 400 cycles (Figure 1d,e) shows that BE results in a larger overpotential of LCO compared with TPF-BE. Thus, it can be speculated that TPF can effectively construct a stable interface to reduce the surface polarization of the LCO cathode. Lowered polarization will further accelerate the diffusion kinetics of Li ions; thus, the galvanostatic intermittent titration technique (GITT) was applied to compare the Li⁺ diffusion kinetics of the LCO cathode in the BE and TPF-BE electrolytes during the charging and discharging process. As presented in Figure S4, the LCO cathode with TPF-BE exhibits higher Li⁺ diffusion coefficients (D_{Li}^+) at the highvoltage range, indicating that the introduction of the TPF additive accelerates the diffusion of Li+ in LCO at deep delithiated states. To further verify the enhanced interfacial kinetics, in situ galvanostatic electrochemical impedance spectroscopy (in situ GEIS) was applied to detect the interfacial resistance evolution of the LCO cathode. As

presented in Figure S5, after charging to 4.4 V, the R_{ct} values of the LCO cathode in both BE and TPF-BE increase significantly. However, it is noteworthy that the R_{ct} value measured in TPF-BE is always lower than that in BE during the whole charging process, especially in the high-voltage range, which is consistent with the GITT results. Cycled electrochemical impedance spectroscopy (EIS) results of coin cells in both electrolytes also show that TPF-BE enables lower interfacial resistances compared with BE, providing faster transferring kinetics (Figure S6). This phenomenon can be attributed to the formation of a more stable cathodeelectrolyte interphase (CEI) with higher Li⁺ diffusion kinetics, as evidenced by the distribution of relaxation times (DRT) analysis (Figure S7). As shown in Figure S8, a more distinct signal corresponding to the CEI formation was observed in the cyclic voltammetry (CV) curves using the TPF-BE electrolyte compared with the BE, further confirming the enhanced interfacial stability by TPF-induced CEI formation. Benefiting from the lower polarization and faster Li⁺ diffusion kinetics, TPF-BE exhibits much-improved rate performance compared to BE. As presented in Figure 1f, although BE and TPF-BE show similar discharge specific capacity at low C rates (0.1 and 0.2C), as the current density further increases, TPF-BE maintains a higher capacity than BE. During the ultrafast charge and discharge process at 30C, TPF-BE can still deliver a specific capacity of 90 mAh g⁻¹, which is much higher than the value obtained from BE (12 mAh g^{-1}).

In order to evaluate the electrochemical enhancement effect of the TPF additive on full cells, proof-of-concept LCOllSiO $_x$ pouch cells were assembled, and the cycle performance tests were carried out under 1C. As shown in Figure 1g, the pouch full cell using the TPF-BE electrolyte exhibits significantly improved cycle stability, whereas the capacity of the pouch cell using BE decreases sharply after 60 cycles, which originates from the continuous side reactions that consume a large amount of the electrolyte, resulting in a rapid rise of cell internal resistance. ³¹

2.2. Theory and Characterization of the B-O **Complexing Interface.** The cyclic voltammetry (CV) curves of the LCO cathode in the voltage range of 3-4.6 V (Figure S8) show that TPF-BE results in an additional oxidation peak at \sim 3.3 V during the initial two cycles. Combined with the observation of electrochemical curves in the first cycle (Figure 1a) that TPF-BE results in a higher charge specific capacity, it can be reasonably speculated that the TPF additive undergoes oxidative decomposition reactions during the charging process and participates in the in situ formation of the CEI layer on the LCO cathode surface. Furthermore, the components of the constructed interface were revealed via spectroscopy analysis. First, X-ray photoelectron spectrometry (XPS) was utilized to detect the C 1s, B 1s, and F 1s spectra of the LCO cathode surface after 100 cycles in BE and TPF-BE. The comparison of B 1s spectra demonstrates that the TPF additive introduces boron-containing species in the CEI layer on the LCO surface (Figure 2a,b), which is conducive to Li⁺ transfer at the

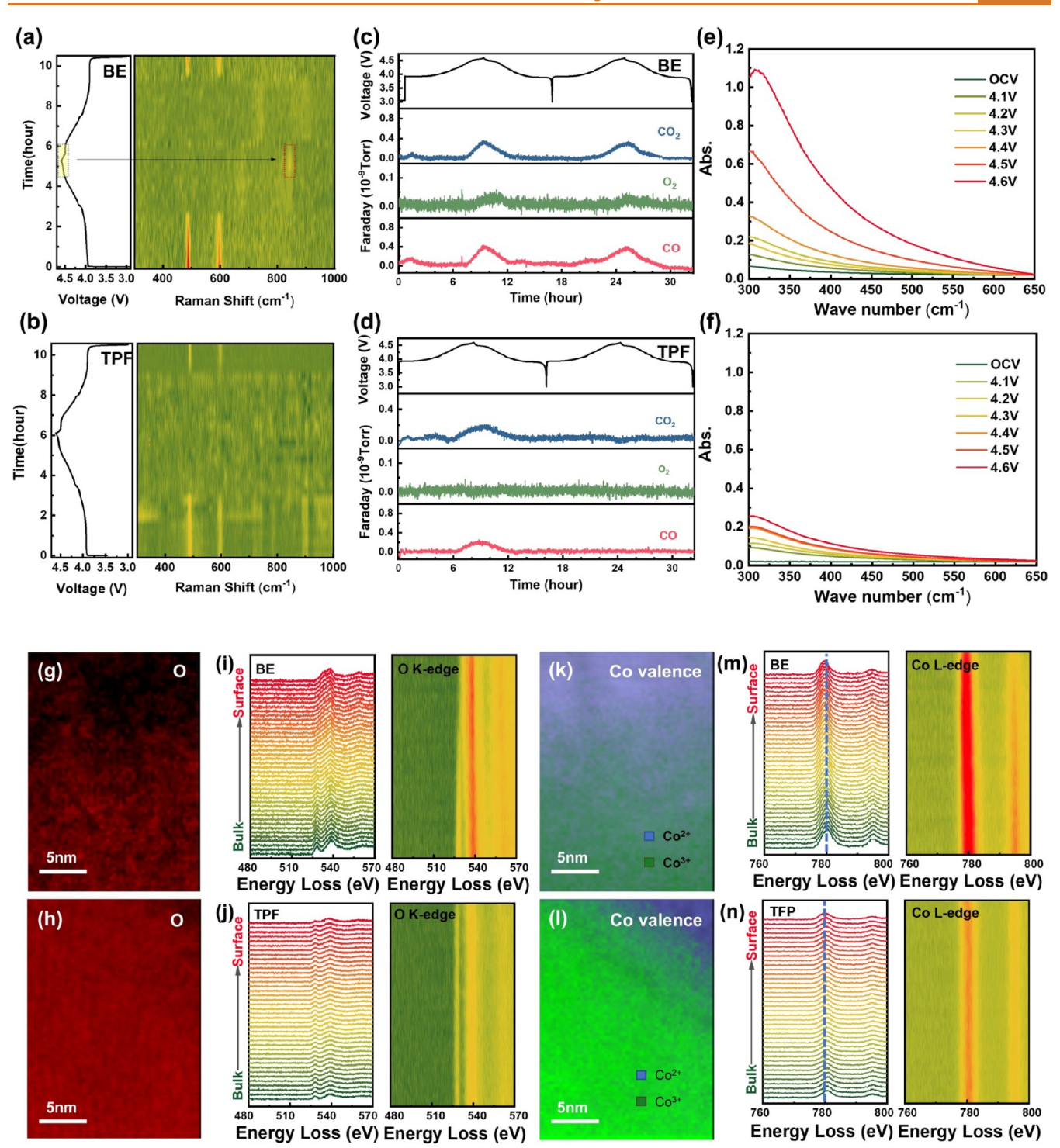


Figure 3. In situ interfacial characterization and chemical states of the O and Co elements. In situ SHINERS results of the LCO cathode in BE (a) and TPF-BE (b). differential electrochemical mass spectrometry (DEMS) measuring results of the LCO cathode in BE (c) and TPF-BE (d). In situ ultraviolet—visible (UV—vis) results of the LCO cathode in BE (e) and TPF-BE (f). Electron energy loss spectroscopy (EELS) mapping results of the O element distribution in BE (g) and TPF (h); EELS spectra of the O K-edge in BE (i) and TPF (j); the valence distribution of the Co element in BE (k) and TPF (l); and EELS spectra of the Co L-edge in BE (m) and TPF (n) of the LCO cathode from the bulk to the surface after 100 cycles.

electrode/electrolyte interface. The O 1s spectra show that a weakened signal corresponding to lattice oxygen appeared in the presence of the TPF additive (Figure 2c,d), indicating that the TPF-derived byproducts form a more uniform and compact CEI on the LCO surface, thereby suppressing interfacial degradation. It is also worth noting that in the F

Is spectrum, the content of LiF (685.5 eV) on the surface obtained in TPF-BE (Figure S9a) is significantly higher compared with the BE (Figure S9b). Therefore, it could be speculated that the additional F atoms in TPF lead to a LiFrich CEI layer on the LCO surface upon its oxidation, which is beneficial for the stability of the CEI layer during high-voltage

operations.³² However, the relative contents of components such as C–O, C=O, CO₃, and C–F in the C 1s spectrum peaks are basically identical in both electrolytes (Figure S9c,d), indicating that TPF does not affect the formation of components such as ROCO₂Li, LiCO₃, and polycarbonate.³³ The transmission electron microscopy (TEM) image also shows a uniform amorphous CEI layer on LCO cycled in TPF-BE, supporting the formation of a stable and compact interphase (Figure S10).

Next, time-of-flight secondary ion mass spectrometry (TOF-SIMS) was carried out to reveal the spatial distribution of various surface CEI layer components formed in BE and TPF-BE electrolytes (Figure 2e,f). The generation of $-CoF_2^+$ fragments can be attributed to the corrosion reaction between HF and LCO;³⁴ thus, the lower content of -CoF₂⁺ on the surface of LCO in TPF-BE indicates that the corrosion reactions of HF toward the LCO surface have been effectively inhibited (Figure S11). In addition, similar to the results of the F 1s spectrum in XPS, -LiF₂⁻ fragment (corresponding to the LiF component) distributions show that the surface of the cathode in TPF-BE is uniformly covered with a higher content of LiF than BE (Figure 2g,h). Moreover, a dense yet thin layer consisting of -BO⁺ and -Li₂BO₂⁺ fragments were observed on the surface of LCO (Figure 2h), which is consistent with the XPS result (Figure 2b). Since there is no B-O bond in TPF, the newly emerged B-O bonds right on the top of the LCO surface suggest the interaction between boron and oxygen on the LCO surface (Figure 2f). The energy-dispersive spectroscopy (EDS) results presented in Figure S12 also verify that the B and F elements distribute evenly on the surface of cycled LCO particles in TPF-BE, which correspond to the Bcontaining species and LiF or F-containing species in the CEI layer, respectively. These results collectively indicate that the LiF and B-O containing species function synergistically in stabilizing the interface.

Based on the electronic structure of B (1s²2s²2p¹) and its coordination ability with oxygen, and the interactions between B and O on the LCO surface validated by TOF-SIMS results (Figure 2f,h), it is reasonable to speculate that the lattice oxygen of LCO may be complexed with derived boron species from the TPF-based electrolyte, further contributing to the stabilization of the electrode-electrolyte interface. To verify the speculation, density functional theory (DFT) calculations were employed to theoretically investigate the interfacial evolution of TFP at the LCO interface. As shown in Figure S13, the TPF additive exhibits a positive adsorption energy (0.88 eV) on the LiCoO₂ surface, manifesting the difficulty of TPF adsorption on LiCoO₂ before electrochemical chargedischarge. However, the decomposed components of the TFP additive exhibit stronger adsorption on the LCO surface at various delithiation stages (Figures 2i,j and S14-S18), indicating a preferential interaction with the electrode surface compared with EC, dimethyl carbonate (DMC), and diethyl carbonate (DEC) solvents. Especially, the decomposed products of TPF display lower adsorption energy through B-O complexing with Li_xCoO_2 (x = 1, 0.5, 0) than C-O coordination (Figures S14, S16, and S17). For instance, ringstructural R-CFB exhibits an absorption energy of -6.11 eV on Li_{0.5}CoO₂ through B-O complexing, lower than that for similar ring-structural R-CF without B atoms (-2.94 eV); Figure S16). This comparison underscores the critical role of boron in enabling strong B-O coordination, which anchors TPF-derived fragments to the LCO surface more effectively

than their B-free analogs. The presence of fluorine-containing boron species, compared to fluorinated carbon-only species, leads to more stable interfacial binding, thus contributing to the suppression of interfacial oxygen evolution and enhancing cathode stability. Since the TPF additive only contains B, C, and F atoms (Figure S1), preferential B-O complexing between TPF decomposed products with the LCO surface at various delithiation stages was validated. Furthermore, the absorption configurations also influence the oxygen vacancy formation energy of LiCoO₂ during delithiation (Figure 2k). Notably, the delithiated LCO surface in the presence of the TPF-derived components demonstrates higher oxygen vacancy formation energies than EC, DMC, and DEC solvents (Figures 2k and S19-S21), indicating enhanced lattice oxygen stabilization and a protective effect of the TPF-derived species on the structural integrity of LCO. The enhanced lattice oxygen stabilization was correlated with B-O complexing provided by TPF-derived products with LCO and induced a lower projected density of states (PDOS) of oxygen atoms (Figures 21–n and S22). It has been reported that in LiCoO₂ cathodes, elevated oxygen 2p states near the Fermi level are strongly associated with anionic redox activity and lattice oxygen evolution. In contrast, the PDOS analysis in this work reveals a suppressed oxygen electronic state density near the Fermi level, which is attributed to the presence of TPF-derived B-O complexes. 35,36 This indicates a distinct mechanism that effectively stabilizes lattice oxygen by lowering its electronic reactivity.

From above, by combining the experimental results (TOF-SIMS, XPS, and EDS) and theoretical calculations, preferential absorption of TPF-derived species on the LCO surface at different delithiation states to form interfacial B—O complexing was validated. Such B—O complexing leads to a lower PDOS of oxygen and a higher oxygen vacancy formation energy for LCO.

2.3. Effects of B-O Complexing on Interfacial **Evolution.** In order to explore the electrochemical performance improvement mechanisms of LCO by the constructed B-O complexing interface, in situ characterization methods were conducted. First, in situ shelled-isolated nanoparticle-enhanced Raman spectroscopy (in situ SHINERS) was applied to capture the oxidation products of lattice oxygen on the surface of LCO cathodes. As presented in Figure 3a,b, the Raman signal variations of the LCO surface during the initial cycle in BE and TPF-BE were collected. The Raman peaks located at 485 and 595 cm⁻¹ correspond to the bending vibration (E_g) and Co-O stretching vibration (A_{1g}) of the O-Co-O bond in the O3 layered LCO cathode, respectively.³⁷ As the potential reaches 4.1 V, the peak signals of E_{g} and A_{1g} in both electrolytes disappear and gradually recover when the potential reduces back to 3.95 V, indicating a reversible breakingrecovering process of O-Co-O and Co-O bonds on the surface of LCO during high-potential operations.³⁸ It is worth noting that in BE, when LCO was charged to 4.5 V, a new Raman vibration peak appeared at ~843 cm⁻¹, corresponding to the stretching vibration of the O-O bond of the peroxygenlike compound (O22-) generated by the oxidation of lattice oxygen.³⁹ By contrast, no obvious O₂²⁻ oxidation products were observed on the surface of LCO in TPF-BE. Considering the lower PDOS of oxygen after B-O complexing (Figure 2n) and the electronic structure of B (1s²2s²2p¹) with electronwithdrawing property, it is rational to speculate that the B-O complex bonds at the interface effectively stabilized the lattice

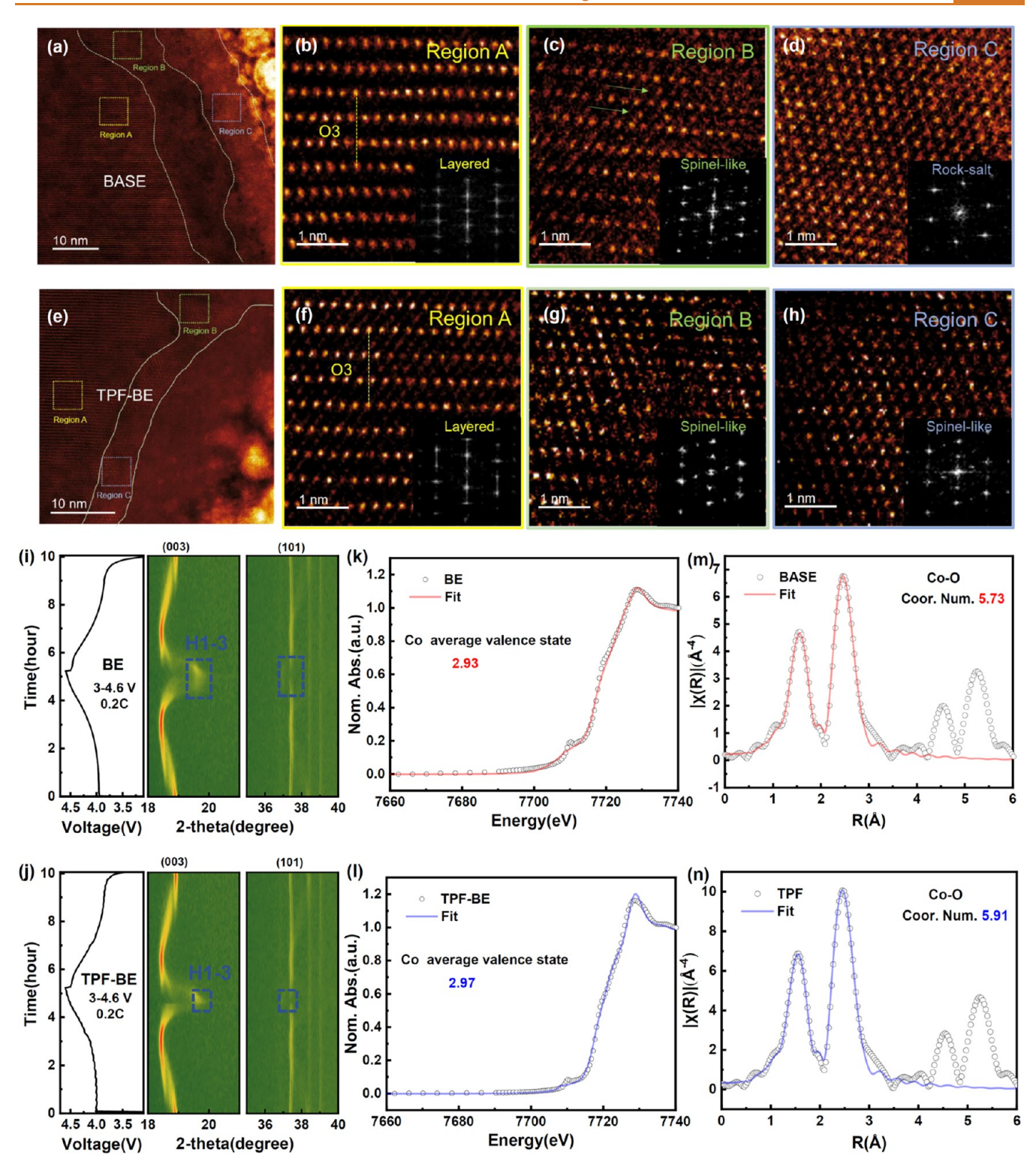


Figure 4. Structural characterization of the LCO cathode. HADDF-STEM images and the FFT diffraction patterns of the selected region of LCO cathodes after 100 cycles in BE (a-d) and TPF-BE (e-h). In situ X-ray diffraction (XRD) results of the LCO cathode in BE (i) and TPF-BE (j). X-ray absorption near-edge structure (XANES) measuring and fitting results of LCO cathodes after 100 cycles in BE (k) and TPF-BE (k). Extended X-ray absorption fine structure (EXAFS) measuring and fitting results of LCO cathodes after 100 cycles in BE (k) and TPF-BE (k).

oxygen on the surface of LCO and inhibited its oxidation into an O_2^{2-} compound at high voltages.

Since the peroxygen-like $(O_2^{\ 2^-})$ compound can be further oxidized to generate O_2 and react with solvent to produce CO_2 and CO_2 resulting in the loss of O on the surface of the

cathode material, ¹⁸ differential electrochemical mass spectrometry (DEMS) was applied to compare the gas release of LCO cathodes in both electrolytes. As shown in Figure 3c,d, when first charged to 4.3 V, the cell using BE produces more CO₂ and CO than TFP-BE, showing more drastic decomposition

reactions of the electrolyte during the first cycle. In the second cycle, thanks to the protective effect of the B–O complexing interface generated by the TPF additive on the LCO cathode, no obvious generation of CO_2 and CO can be detected in TPF-BE. Contrarily, in BE, CO_2 and CO continued to appear in the high-voltage region, indicating uncontrolled electrolyte decomposition. Moreover, the signal of O_2 can only be detected in BE, which is in accordance with the in situ SHINERS results, further confirming that the functional interface can stabilize surface lattice oxygen by forming B–O complex bonds, preventing the irreversible oxidation reaction of lattice oxygen.

As the lattice oxygen escapes from the LCO lattice structure, cobalt in the transition metal layer also becomes unstable. To investigate the stability of cobalt in LCO at high voltages, we applied in situ ultraviolet-visible (in situ UV-vis) spectroscopy to measure Co dissolution from LCO into electrolytes. The in situ UV-vis spectra (Figure 3e,f) show that during the charging process, the absorption peak intensity of dissolved Co in TPF-BE is significantly lower than that in BE, suggesting that Co dissolution can be mitigated by TPF, in good agreement with the TOF-SIMS results (Figure 2e,f). In addition, it is worth noting that in BE, the intensity of the Co absorption peak increases sharply when the voltage reaches 4.5 V (Figure 3e), which may be related to the formation of O₂²⁻ species, hence the accelerated Co dissolution. This phenomenon is dramatically inhibited in the presence of TPF (Figure 3f), indicating that the CEI layer formed by the TPF additive could stabilize the Co element by anchoring the lattice oxygen.

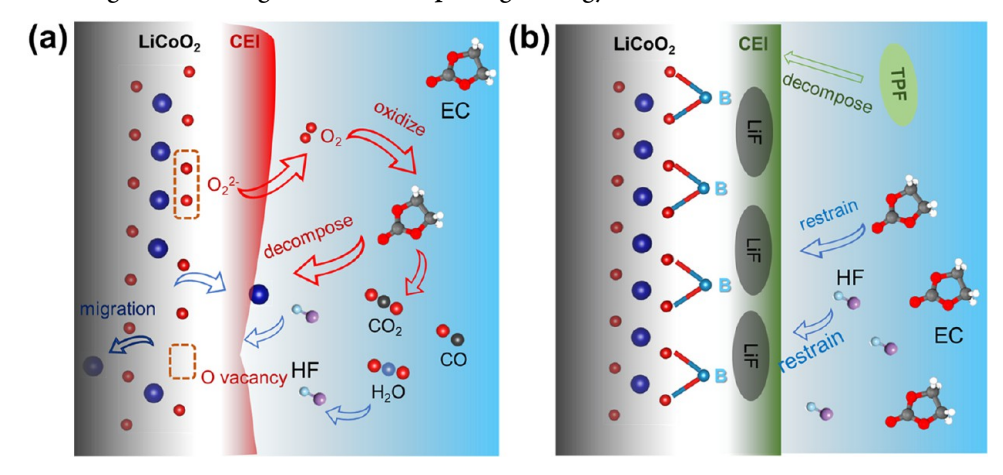
To probe the chemical states of Co on the surface of LCO, map scanning of electron energy loss spectroscopy (EELS) was applied to detect the distribution of O and Co and the valence distribution of the Co element at the near-surface area of cycled LCO particles. Obviously, as presented in Figure 3g, there are a large number of oxygen vacancies on the surface of LCO particles after long cycling in BE due to the irreversible oxidation of oxygen species. Some of the oxygen vacancies can be observed in the bulk phase, indicating that the oxygen vacancies generated by oxygen loss on the surface of LCO have migrated to the bulk phase.²⁷ This result was confirmed by the line scanning results of LCO cycled in BE (Figure 3i): the intensity of the front-edge peak at ~530 eV in the O K-edge EELS spectrum gradually weakens from the bulk to the surface, corresponding to the higher concentrations of the O vacancies on the surface of LCO.⁴⁰ In sharp contrast, the distribution of O element in TPF-BE is homogeneous without obvious O loss (Figure 3h), and line scanning results of front-edge peak from bulk to surface (Figure 3j) also exhibit constant intensity, indicating that the lattice O is well protected owing to the B-O complexing interface. In addition, compared with the LCO particles in TPF-BE (Figure S23a,c), the signal intensity of the Co element on the surface of the LCO particles in BE is much weaker (Figure S23b,d), corresponding to the more severe Co dissolution near the surface. Moreover, the valence distribution of Co obtained by fitting the EELS standard spectrum further reveals that there is a large amount of reduced Co²⁺ near the surface of LCO after long cycling in BE (Figure 3k). The line scanning results of the Co L-edge of LCO at ~780 eV gradually shift to lower energy from the bulk to the surface, verifying the reduction of the valence state (Figure 3m). Thus, it can be speculated that the lattice oxygen loss may also cause the valence reduction of cobalt in order to maintain electrical

neutrality.⁴¹ The valence change of the Co element may further cause the irreversible phase transition and capacity decay, which will be discussed in the following paragraphs. In contrast, thanks to the stabilized lattice oxygen in TPF-BE, most Co element near the surface of the LCO particles still remains Co³⁺ (Figure 3l). The corresponding line scanning results of the Co L-edge in TPF-BE also exhibit an unchanged valence state of Co from the bulk to the surface (Figure 3n).

2.4. Effects of B-O Complexing on the Bulk **Structure.** To unveil the impacts of interfacial reconstruction on the bulk structure of LCO, we first applied high-angle annular dark-field scanning transmission electron microscopy (HADDF-STEM) to detect the crystalline structure of cycled LCO in both electrolytes. With the help of the fast Fourier transform (FFT) diffraction patterns, it can be observed that LCO cycled in BE exhibits three layers of structures from the surface to the bulk (Figure 4a), which are the outermost rocksalt phase (Figure 4d), the near-surface spinel-like phase (Figure 4c), and the innermost layered phase (Figure 4b). The thicknesses of both the rock-salt phase and the spinel-like phase layer are about 10 nm. In comparison, a spinel-like phase layer with a thickness of about only 5 nm can be found on the surface of LCO cycled in TPF-BE (Figure 4e,g,h), and the rest of the bulk still remains in the layered phase (Figure 4f), indicating that the TPF additive has an obvious effect on inhibiting the irreversible phase transition from the layered phase to the spinel-like and rock-salt phases of the LCO cathode material during prolonged cycling.

In order to further investigate the mechanism of phase transition, in situ X-ray diffraction (XRD) was applied to real time observe the long-term structure evolution of LCO during charge and discharge (Figure 4i,j). For both electrolytes, the (003) peak of LCO shifts to a higher angle during the charging process, corresponding to the formation of O3-II/III, and its shift to lower angles at a high-voltage range can be attributed to the formation of H1-3 phases. 42 It can be observed that the H1-3 phase appears after charging to 4.46 V and disappears after discharging to 4.42 V in BE; in comparison, its appearance is postponed to 4.53 V and its disappearance is brought forward to 4.50 V in TPF-BE. Because the transition from the O3 phase to the H1-3 phase is accompanied by drastic structural distortion and slippage of the O-Co-O lattice planes, 43 the shortened existing period of the H1-3 phase in TPF-BE can be related to the suppressed generation of O vacancies and migration of Co ions, which further inhibits the slippage of the oxygen layer. In addition, less formation of the H1-3 phase in the high-voltage range also contributes to the faster Li⁺ diffusion coefficients, as demonstrated in Figure S4. Since the H1-3 phase is typically accompanied by lattice oxygen release and cobalt migration into the Li layers, its suppression suggests that the TPF-derived B-O complexing layer effectively stabilizes the interfacial and bulk structures. Further comparison of the XRD patterns of LCO after long cycling is further presented in Figure S24a, where the (003) peak obtained in BE exhibits weaker intensity and shifts to higher angles compared with that obtained in TPF-BE. The refined results of XRD data (Figure S24b,c) show that the LCO material cycled in BE contained 2.86% Co₃O₄ spinel phase, which was significantly higher than that in TPF-BE (0.97%). Since the formation of the spinel phase is usually associated with the O vacancy-induced migration of Co ions from the transition metal layer to the Li layer, ²⁷ the suppressed

Scheme 1. Schematic Diagrams Showing the B-O Complexing Strategy to Stabilize the LCO Cathode/Electrolyte Interface



"(a) Interfacial interactions with the BE electrolyte, leading to surface lattice oxygen loss and Co ion migration; (b) interfacial interactions with the TPF electrolyte additive, leading to B-O complexing and LiF-rich CEI constructed on the LCO surface.

Co₃O₄ formation in TPF-BE can be attributed to the stabilized surface lattice oxygen by the B–O complexing interface.

Next, the X-ray absorption near-edge structure (XANES) spectra of the Co K-edge of the LCO cathode after 100 cycles were collected to measure the Co average valence states. Through linear fitting of the XANES spectra, the average valence states of Co after cycling in BE and TPF-BE are 2.93 (Figure 4k) and 2.97 (Figure 4l), respectively. Based on these values, it can be estimated that ~7% Co³⁺ is reduced to Co²⁺ in LCO after 100 cycles in BE, while only ~3% of Co³⁺ is reduced in TPF-BE, which agrees with the EELS data presented in Figure 3k,l.

To determine the local coordination structure, we collected the extended X-ray absorption fine structure (EXAFS) spectra of the Co K-edge of the LCO cathodes cycled in both electrolytes. By fitting the spectral peaks of Co-O and Co-Co/Li bonds in the range of atomic spacing from 1 to 3 Å, the Co-O coordination numbers of LCO cycled in BE and TPF-BE electrolytes are calculated to be 5.73 (Figure 4m) and 5.91 (Figure 4n), respectively. Compared with the theoretical value (i.e., 6), the lower Co-O coordination number obtained in BE can be ascribed to the generation of a large number of oxygen vacancies and the phase transition to the Co₃O₄ spinel phase with partial tetracoordinated Co-O bonds. In comparison, the LCO cathode cycled in TPF-BE possesses a relatively higher Co-O coordination number that is close to the initial structure, demonstrating less distortion in local structures. To further validate the lattice oxygen stability, O K-edge soft X-ray absorption spectra were recorded in fluorescence mode after long-term cycling (Figure S25). Notably, the TPFcontaining electrolyte exhibits a stronger and better-preserved lattice oxygen signal at ~529.5 eV compared to the baseline, corroborating the mechanism that TPF effectively suppresses oxygen evolution and enhances structural stability under highvoltage operation.

3. CONCLUSIONS

In this study, by using tris(pentafluorophenyl)borane as an electrolyte addition, we constructed a B–O complexing interface to stabilize the lattice oxygen of LCO at 4.6 V, in which the surface lattice oxygen in LCO preferentially coordinated with B atoms in TPF additive-derived products. Combining theoretical calculations with various spectral and

electron microscopy characterization methods, it was revealed that the B-O complexing interface can efficiently reduce the PDOS of oxygen in LCO, inhibiting the emergence of peroxylike species above 4.5 V, avoiding the irreversible O loss. Benefited from the resulted less oxygen vacancies, the Co migration in the LCO lattice, Co dissolution in the electrolyte, and valence reduction have been suppressed (Scheme 1), drastically retarding adverse phase transition and local coordination structure change. Besides, benefiting from fluorine-containing groups in the TPF additive, LiF-rich CEI was constructed on the LCO surface. Such a B-O complexing and LiF-rich interface eventually delivers higher cycling stability during prolonged high-voltage operation. This work studied in depth the mechanism of how the interfacial B-O complexing strategy stabilizes the lattice oxygen of LCO, which not only provides a perspective on the origin of instability of LCO cathode but also sheds light on how to construct a stable interface for high-voltage layered cathodes (i.e., Ni-rich, Lirich, etc.).

4. METHODS/EXPERIMENTAL SECTION

- **4.1. Electrolytes and Electrode Preparation.** The base electrolyte contained 1 M LiPF₆ in EC/DMC/DEC (1:1:1, by volume ratio). Tris(pentafluorophenyl)borane (99%, Aladdin) as an additive was introduced into the base electrolyte to obtain the TPF-BE electrolyte. The positive electrodes were fabricated with the LiCoO_2 active material (purchased from Xiamen Tungsten New Energy Material Corporation), acetylene black (AB), and poly-(vinylidene fluoride) (PVDF, 8:1:1, by mass ratio). The anode electrode utilized in the full cell was fabricated with a SiO_x active material (purchased from BTR New Material Group), AB, and sodium carboxymethyl cellulose (CMC, 8.5:1:0.5, by mass ratio).
- **4.2. Electrochemical Measurement.** The LillLiCoO₂ half-cell was assembled with a LiCoO₂ cathode, lithium metal, a Celgard film, and 60 μ L of the electrolyte in an Ar-filled glovebox. The SiO_xll LiCoO₂ full cell was assembled into a pouch cell with dimensions of 5.6 cm × 3.3 cm in the pouch cell production line. A LiCoO₂ cathode with a mass loading of ~16.5 mg cm⁻² and a SiO_x-based anode (~7.5 mg cm⁻²) were employed. Prior to assembly, the SiO_x anode was prelithiated by direct contact with lithium metal foil for 12 h. The capacity ratio of negative electrode capacity/positive electrode capacity (N/P ratio) was 1.12:1. The galvanostatic electrochemical measurements were carried out with a NEWARE battery test system at 25 °C. Prior to the galvanostatic intermittent titration technique (GITT) test, the LillLiCoO₂ half-cell was precycled 3 times and then

tested with the procedure of charging/discharging for 1 min and standing for 2 h in a micro-electrochemical workstation. The cyclic voltammetry (CV) and linear sweep voltammetry (LSV) tests were utilized as a three-electrode system containing LiCoO₂ (for CV) and stainless steel (for LSV) as the work electrode, lithium metal as the counter electrode, and Pt as the reference electrode through a Solartron Analytical 1470E electrochemical workstation at a scan rate of 0.1 mV s⁻¹. The ex situ electrochemical impedance spectroscopy (EIS) data after different cycles were collected from the LillLiCoO₂ half-cell with 100% SOC at a frequency range of 100 kHz to 0.01 Hz on a Solartron Analytical 1470E electrochemical workstation. For in situ galvanostatic electrochemical impedance spectroscopy (GEIS), to eliminate the effect of anode potential change, Pt was used as a reference electrode to correct the positive potential. The GEIS data were synchronously collected at a frequency range of 10 kHz to 0.05 Hz along with a galvanostatic charging/discharging between 3 and 4.6 V at 25 mA g⁻¹

- **4.3. DFT Calculation.** All of the DFT⁴⁴ calculations were implemented in the Vienna Ab initio Simulation Package (VASP)⁴⁵ with the projector augmented method. The electron wave function of valence electrons was expanded using the projected augmented wave (PAW) basis set. We employed the generalized gradient approximation (GGA)⁴⁶ level of DFT + D3 with the Perdew–Burke–Ernzerhof (PBE)⁴⁷ exchange-correlation functional to describe the exchange-correlation effects in this study. The plane wave truncation energy of 520 eV and the system's total energy of less than 1.0×10^{-5} eV were utilized for all the calculations. To describe on-site Coulomb interactions, all elementary reaction steps were calculated using the DFT + U method, with a U value of 4.0 eV for Co 3d, which was determined using the tetrahedron integration method. The γ k-point sampling method was carried out for all calculations with $1 \times 1 \times 1$ k-point samplings.
- **4.4. Material Characterization.** *4.4.1. FT-IR.* The Fourier transform infrared (FT-IR) spectra of the electrolytes were collected on an infrared spectrometer in an Ar-filled glovebox (Thermo Fisher Scientific iN10).
- 4.4.2. XPS. The X-ray photoelectron spectra were collected on a Thermo Scientific Escalab 250Xi spectrometer. The obtained spectra were calibrated by a C 1s signal at 284.8 eV.
- 4.4.3. EDS. The elemental distribution investigation of the samples was conducted using an energy-dispersive spectroscopy (EDS) detector (Oxford X-Max20).
- 4.4.4. TOF-SIMS. The time-of-flight secondary ion mass spectra (TOF-SIMS) were performed by a PHI nano TOF II spectrometer equipped with a bismuth primary ion source and a Cs⁺ sputter source for probing the fragment ions. A Bi³⁺ beam (30 kV) was used as the primary beam to detect the samples. The unbunched mode (UB mode) was also employed to obtain results with higher spatial resolution.
- 4.4.5. Hard X-ray Absorption Spectra (hXAS). The hard X-ray absorption spectra (hXAS) measurements were conducted at the 1W1B station at the Beijing Synchrotron Radiation Facility (BSRF). The fitting of the X-ray absorption fine structure (XAFS) and extended X-ray absorption fine structure data (EXAFS) were performed by Athena and Artemis software, respectively.
- 4.4.6. Soft X-ray Absorption Spectra (sXAS). The soft X-ray absorption spectra (sXAS) measurements were conducted at the Shanghai Synchrotron Radiation Facility (SSRF) "In Situ Soft X-ray Spectroscopy Beamline" (31124.02.SSRF.BL02B02). The incidence angle was 90°.
- 4.4.7. Cryogenic Transmission Electron Microscopy (Cryo-TEM). Cryo-TEM images were collected on a JEM-100F microscope. The LiCoO₂ particles after 100 cycles were scraped from the electrode sheets, rinsed with dimethyl carbonate (DMC), and then loaded on an ultrathin carbon film (Ted Pella, Inc., USA). It was transferred into a Gatan side-entry cryo-transfer holder (Gatan model 910) in an Arfilled glovebox and sealed inside the holder. The cryo-TEM holder was quickly inserted into a JEM-100F microscope, and the temperature of the sample was dropped and stabilized at $-178\ ^{\circ}\mathrm{C}$ by immersion in liquid nitrogen.

- 4.4.8. HADDF-STEM and EELS. The samples for high-angle annular dark-field scanning transmission electron microscopy (HADDF-STEM) and electron energy loss spectra (EELS) were prepared using a focused ion beam (FIB, FEI Scios). The HADDF-STEM images were taken using an FEI Tecnai G2 F30 microscope. The EELS map scanning and line scanning data were collected through a Continuum 1069HR electronic energy loss spectrometer. The data were analyzed using Digital Micrograph (Gatan) software.
- 4.4.9. Raman. All of the Raman spectra were performed on a Renishaw in Via Raman spectrometer with a 633 nm wavelength laser. The laser beam power delivered to the sample surface was 10% of the maximum 17 mW intensity. To obtain the Raman spectra of the electrolyte, the electrolyte was sealed in a 2032-type coin cell with a small hole covered by a 2 mm thick sapphire.
- 4.4.10. In Situ SHINES. To collect core—shell separation nanoparticle-enhanced Raman signals (SHINES), $Au@SiO_2$ nanoparticle-dispersed solution (PERSER-TECH, CP-2) was dropped onto the cathode surface and dried in vacuum. The cathode was assembled at the bottom of a CR-2032 coin cell with active materials facing upward. The membrane, Li metal, and cell cover were punched with a small hole in the center, and a 2 mm thick sapphire was covered on top of the cell for signal collection. The galvanostatic charge—discharge process was carried out using a NEWARE battery test system at 40 mA g⁻¹.
- 4.4.11. XRD. All of the X-ray diffraction (XRD) patterns were obtained using a Bruker D8 Advance diffractometer (Cu K α radiation, $\lambda = 0.154$ nm). Rietveld refinements of XRD patterns were performed by using GSAS software packages.
- 4.4.12. In Situ XRD. To collect operator XRD patterns, the cathode slurry was coated onto a 7 μ m thick Al foil to reduce the signal blocking. The LiCoO₂ cathode was assembled on the top of a CR-2032 coin cell with the active material facing downward. The cell cover was punched with an 8 mm diameter hole covered with a 5 μ m thick polyimide membrane. The electrochemistry was performed using a NEWARE battery test system. The assembled coin in situ cell was first cycled for 5 cycles at a current density of 0.1C to construct a stable CEI layer, and then in situ XRD tests were performed at a current density of 0.2C.
- 4.4.13. In Situ DEMS. The in situ differential electrochemical mass spectrometry (DEMS) experiments utilized an ECC-DEMS cell (ELCELL) and online mass spectrometry (HPR-20 EGA). During the DEMS test, the in situ cell was continuously purged with Ar gas at a flow rate of 0.5 sccm. The galvanostatic charge—discharge process was carried out using a NEWARE battery test system at 25 mA $\rm g^{-1}$.
- 4.4.14. In Situ UV-Vis. The in situ ultraviolet-visible spectrum (UV-vis) tests were carried out using a quartz cuvette assembled with a cathode, Li metal, a Celgard film, and 1.5 mL of the electrolyte on a UV-vis spectrometer (Shimadzu UV2600). The potential was driven by a Solartron Analytical 1470E electrochemical workstation.

ASSOCIATED CONTENT

Data Availability Statement

The data that support the findings of this study are available from the corresponding author upon reasonable request.

Supporting Information

The Supporting Information is available free of charge at https://pubs.acs.org/doi/10.1021/acsnano.5c11997.

Electrolyte characterization (Raman, FT-IR, UV-vis, NMR, and LSV); electrochemical results (GITT, CV, galvanostatic cycling, in situ/variable-temperature EIS, GEIS, and DRT); surface/interface analyses (XPS, cryo-TEM, TOF-SIMS, EDS, and EELS); DFT calculations of adsorption energies and oxygen vacancy formation; PDOS analysis; and structural characterization (XRD, in situ XRD, hXAS, and sXAS) (PDF)

AUTHOR INFORMATION

Corresponding Authors

Yuchen Ji — School of Advanced Materials, Peking University Shenzhen Graduate School, Shenzhen 518055, China; Email: yuchenji@pku.edu

Feng Pan — School of Advanced Materials, Peking University Shenzhen Graduate School, Shenzhen 518055, China; orcid.org/0000-0002-8216-1339; Email: panfeng@pkusz.edu.cn

Zu-Wei Yin — School of Advanced Materials, Peking University Shenzhen Graduate School, Shenzhen 518055, China; College of Energy, Xiamen University, Xiamen 361005, China; orcid.org/0000-0002-0728-1154; Email: yinzuwei@xmu.edu.cn

Authors

Jimin Qiu – School of Advanced Materials, Peking University Shenzhen Graduate School, Shenzhen 518055, China

Wenfang Li — The Extension Service Station of Agricultural Mechanization Technology of Kaiping, Jiangmen 529386, China

Yuhang Li — Shenzhen All-Solid-State Lithium Battery Electrolyte Engineering Research Center, Tsinghua Shenzhen International Graduate School, Shenzhen 518055, China

Wenguang Zhao — School of Advanced Materials, Peking University Shenzhen Graduate School, Shenzhen 518055, China

Yunxing Zuo – Shenzhen Eacomp Technology Co., Ltd., Shenzhen 518052 Guangdong, China

Weiyuan Huang — School of Advanced Materials, Peking University Shenzhen Graduate School, Shenzhen 518055, China

Chen Zhu – School of Advanced Materials, Peking University Shenzhen Graduate School, Shenzhen 518055, China

Mingjian Zhang — School of Advanced Materials, Peking University Shenzhen Graduate School, Shenzhen 518055, China; orcid.org/0000-0002-6843-5911

Guorui Zheng — School of Advanced Materials, Peking University Shenzhen Graduate School, Shenzhen 518055, China

Luyi Yang — School of Advanced Materials, Peking University Shenzhen Graduate School, Shenzhen 518055, China; orcid.org/0000-0002-5516-9829

Complete contact information is available at: https://pubs.acs.org/10.1021/acsnano.5c11997

Author Contributions

[#]J.Q. and Y.J. contributed equally to this work.

Notes

The authors declare no competing financial interest.

ACKNOWLEDGMENTS

This work was supported by the National Natural Science Foundation of China (Nos. 22309153 and 22288102), the Fujian Provincial Natural Science Foundation of China (No. 2024J01040), the Fundamental Research Funds for the Central Universities (No. 20720230039), the Shenzhen Science and Technology Research Grant (JCYJ20200109140416788), and the Soft Science Research Project of Guangdong Province (2017B030301013). The authors thank the support from the Shanghai Synchrotron

Radiation Facility (SSRF, In Situ Soft X-ray Spectroscopy Beamline 31124.02.SSRF.BL02B02).

REFERENCES

- (1) Whittingham, M. S. Ultimate limits to intercalation reactions for lithium batteries. *Chem. Rev.* **2014**, *114* (23), 11414–11443.
- (2) Goodenough, J. B. Evolution of strategies for modern rechargeable batteries. *Acc. Chem. Res.* **2013**, *46* (5), 1053–1061.
- (3) Nitta, N.; Wu, F.; Lee, J. T.; Yushin, G. Li-ion battery materials: present and future. *Mater. Today* **2015**, *18* (5), 252–264.
- (4) Ji, Y.; Huang, Y.; Dong, Z.; Fang, J.; Liu, P.; Liu, S.; Cao, A.; Xue, H.; Chen, S.; Qiu, J.; Du, P. H.; Xie, K.; Xue, S.; Shen, T.; Zheng, G.; Zhao, X.; Yin, Z. W.; Yang, K.; Lin, H.; Xu, K.; Pan, F.; Yang, L. Anion Adsorption at the Inner-Helmholtz Plane Directs Cathode Electrolyte Interphase Formation. *Angew. Chem., Int. Ed.* 2025, 64, No. e202425535.
- (5) Lin, C.; Li, J.; Yin, Z. W.; Huang, W.; Zhao, Q.; Weng, Q.; Liu, Q.; Sun, J.; Chen, G.; Pan, F. Structural Understanding for High-Voltage Stabilization of Lithium Cobalt Oxide. *Adv. Mater.* **2024**, *36* (6), No. e2307404.
- (6) Zhang, J.-N.; Li, Q.; Ouyang, C.; Yu, X.; Ge, M.; Huang, X.; Hu, E.; Ma, C.; Li, S.; Xiao, R.; Yang, W.; Chu, Y.; Liu, Y.; Yu, H.; Yang, X.-Q.; Huang, X.; Chen, L.; Li, H. Trace doping of multiple elements enables stable battery cycling of LiCoO₂ at 4.6V. *Nat. Energy* **2019**, *4* (7), 594–603.
- (7) Qian, J.; Liu, L.; Yang, J.; Li, S.; Wang, X.; Zhuang, H. L.; Lu, Y. Electrochemical surface passivation of LiCoO₂ particles at ultrahigh voltage and its applications in lithium-based batteries. *Nat. Commun.* **2018**, *9*, No. 4918, DOI: 10.1038/s41467-018-07296-6.
- (8) Huang, Y.; Zhu, Y.; Fu, H.; Ou, M.; Hu, C.; Yu, S.; Hu, Z.; Chen, C.-T.; Jiang, G.; Gu, H.; Lin, H.; Luo, W.; Huang, Y. Mg-pillared LiCoO₂: towards stable cycling at 4.6 V. *Angew. Chem., Int. Ed.* **2021**, 60 (9), 4682–4688.
- (9) Xu, S.; Tan, X.; Ding, W.; Ren, W.; Zhao, Q.; Huang, W.; Liu, J.; Qi, R.; Zhang, Y.; Yang, J.; Zuo, C.; Ji, H.; Ren, H.; Cao, B.; Xue, H.; Gao, Z.; Yi, H.; Zhao, W.; Xiao, Y.; Zhao, Q.; Zhang, M.; Pan, F. Promoting surface electric conductivity for high-rate LiCoO₂. *Angew. Chem., Int. Ed.* **2023**, 62 (10), No. e202218595.
- (10) Fu, A.; Lin, J.; Zheng, J.; Wu, D.-Y.; Zhang, Z.; Yan, P.; Su, Y.; Xu, C.; Hao, J.; Zheng, H.; Duan, H.; Ding, Y.; Yan, J.; Huang, S.; Liu, C.; Tang, C.; Fang, X.; Yang, Y. Additive evolved stabilized dual electrode-electrolyte interphases propelling the high-voltage Lill LiCoO₂ batteries up to 4.7 V. *Nano Energy* **2024**, *119*, No. 109095.
- (11) Ren, H.; Hu, J.; Ji, H.; Huang, Y.; Zhao, W.; Huang, W.; Wang, X.; Yi, H.; Song, Y.; Liu, J.; Liu, T.; Liu, M.; Zhao, Q.; Pan, F. Densification of Cathode/Electrolyte Interphase to Enhance Reversibility of LiCoO2 at 4.65 V. Adv. Mater. 2024, 36 (40), No. 2408875, DOI: 10.1002/adma.202408875.
- (12) Yoon, W.-S.; Kim, K.-B.; Kim, M.-G.; Lee, M.-K.; Shin, H.-J.; Lee, J.-M.; Lee, J.-S.; Yo, C.-H. Oxygen Contribution on Li-Ion Intercalation—Deintercalation in LiCoO₂ Investigated by O K-Edge and Co L-Edge X-ray Absorption Spectroscopy. *J. Phys. Chem. B* **2002**, *106* (10), 2526–2532.
- (13) Jiang, Y.; Qin, C.; Yan, P.; Sui, M. Origins of capacity and voltage fading of $LiCoO_2$ upon high voltage cycling. *J. Mater. Chem. A* **2019**, 7 (36), 20824–20831.
- (14) Kong, W.; Zhang, J.; Wong, D.; Yang, W.; Yang, J.; Schulz, C.; Liu, X. Tailoring Co3d and O2p Band Centers to Inhibit Oxygen Escape for Stable 4.6 V LiCoO₂ Cathodes. *Angew. Chem., Int. Ed.* **2021**, *60* (52), 27102–27112.
- (15) Xue, W.; Gao, R.; Shi, Z.; Xiao, X.; Zhang, W.; Zhang, Y.; Zhu, Y. G.; Waluyo, I.; Li, Y.; Hill, M. R.; Zhu, Z.; Li, S.; Kuznetsov, O.; Zhang, Y.; Lee, W.-K.; Hunt, A.; Harutyunyan, A.; Shao-Horn, Y.; Johnson, J. A.; Li, J. Stabilizing electrode—electrolyte interfaces to realize high-voltage LillLiCoO₂ batteries by a sulfonamide-based electrolyte. *Energy Environ. Sci.* **2021**, *14* (11), 6030—6040.
- (16) Wu, Q.; Zhang, B.; Lu, Y. Progress and perspective of high-voltage lithium cobalt oxide in lithium-ion batteries. *J. Energy Chem.* **2022**, 74, 283–308.

- (17) Fang, J.-J.; Du, Y.-H.; Li, Z.-J.; Fan, W.-G.; Ren, H.-Y.; Yi, H.-C.; Zhao, Q.-H.; Pan, F. Surface Structures and Properties of High-Voltage LiCoO₂: Reviews and Prospects. *J. Electrochem.* **2024**, *30* (6), No. 2314005, DOI: 10.61558/2993-074X.3445.
- (18) Zuo, W.; Luo, M.; Liu, X.; Wu, J.; Liu, H.; Li, J.; Winter, M.; Fu, R.; Yang, W.; Yang, Y. Li-rich cathodes for rechargeable Li-based batteries: reaction mechanisms and advanced characterization techniques. *Energy Environ. Sci.* **2020**, *13* (12), 4450–4497.
- (19) Venkatraman, S.; Shin, Y.; Manthiram, A. Phase relationships and structural and chemical stabilities of charged Li_{1-x}CoO₂-delta and Li_{1-x}Ni_{0.85}Co_{0.15}O₂-delta cathodes. *Electrochem. Solid-State Lett.* **2003**, 6 (1), A9–A12.
- (20) Yoon, W. S.; Kim, K. B.; Kim, M. G.; Lee, M. K.; Shin, H. J.; Lee, J. M.; Lee, J. S.; Yo, C. H. Oxygen contribution on Li-ion intercalation-deinterealation in LiCoO₂ investigated by O K-edge and Co L-edge X-ray absorption spectroscopy. *J. Phys. Chem. B* **2002**, *106* (10), 2526–2532.
- (21) Wu, Q.; Zhang, B.; Lu, Y. Progress and perspective of high-voltage lithium cobalt oxide in lithium-ion batteries. *J. Energy Chem.* **2022**, 74 (2), 283–308.
- (22) Xue, W.; Gao, R.; Shi, Z.; Xiao, X.; Zhang, W.; Zhang, Y.; Zhu, Y. G.; Waluyo, I.; Li, Y.; Hill, M. R.; Zhu, Z.; Li, S.; Kuznetsov, O.; Zhang, Y.; Lee, W.-K.; Hunt, A.; Harutyunyan, A.; Shao-Horn, Y.; Johnson, J. A.; Li, J. Stabilizing electrode-electrolyte interfaces to realize high-voltage LillLiCoO₂ batteries by a sulfonamide-based electrolyte. *Energy Environ. Sci.* **2021**, *14* (11), 6030–6040.
- (23) Kong, W.; Zhang, J.; Wong, D.; Yang, W.; Yang, J.; Schulz, C.; Liu, X. Tailoring Co3d and O2p band centers to inhibit oxygen escape for stable 4.6 V LiCoO₂ cathodes. *Angew. Chem., Int. Ed.* **2021**, 60 (52), 27102–27112.
- (24) Xiao, J.; Adelstein, N.; Bi, Y.; Bian, W.; Cabana, J.; Cobb, C. L.; Cui, Y.; Dillon, S. J.; Doeff, M. M.; Islam, S. M.; Leung, K.; Li, M.; Lin, F.; Liu, J.; Luo, H.; Marschilok, A. C.; Meng, Y. S.; Qi, Y.; Sahore, R.; Sprenger, K. G.; Tenent, R. C.; Toney, M. F.; Tong, W.; Wan, L. F.; Wang, C.; Weitzner, S. E.; Wu, B.; Xu, Y. Assessing cathode–electrolyte interphases in batteries. *Nat. Energy* **2024**, 9 (12), 1463–1473.
- (25) Yang, C.; Liao, X.; Zhou, X.; Sun, C.; Qu, R.; Han, J.; Zhao, Y.; Wang, L.; You, Y.; Lu, J. Phosphate-rich interface for a highly stable and safe 4.6 V LiCoO₂ cathode. *Adv. Mater.* **2023**, 35 (14), No. 2210966.
- (26) Ren, X.; Zhang, X.; Shadike, Z.; Zou, L.; Jia, H.; Cao, X.; Engelhard, M. H.; Matthews, B. E.; Wang, C.; Arey, B. W.; Yang, X.-Q.; Liu, J.; Zhang, J.-G.; Xu, W. Designing advanced in situ electrode/electrolyte interphases for wide temperature operation of 4.5 V Lill LiCoO₂ batteries. *Adv. Mater.* **2020**, 32 (49), No. 2004898, DOI: 10.1002/adma.202004898.
- (27) Sun, C.; Liao, X.; Xia, F.; Zhao, Y.; Zhang, L.; Mu, S.; Shi, S.; Li, Y.; Peng, H.; Van Tendeloo, G.; Zhao, K.; Wu, J. High-voltage cycling induced thermal vulnerability in $LiCoO_2$ cathode: cation loss and oxygen release driven by oxygen vacancy migration. *ACS Nano* **2020**, *14* (5), 6181–6190.
- (28) Qin, N.; Gan, Q.; Zhuang, Z.; Wang, Y.; Li, Y.; Li, Z.; Iftikhar, H.; Zeng, C.; Liu, G.; Bai, Y.; Zhang, K.; Lu, Z. Hierarchical doping engineering with active/inert dual elements stabilizes LiCoO₂ to 4.6 V. Adv. Energy Mater. **2022**, *12* (31), No. 2201549.
- (29) Zhuang, Z.; Wang, J.; Jia, K.; Ji, G.; Ma, J.; Han, Z.; Piao, Z.; Gao, R.; Ji, H.; Zhong, X.; Zhou, G.; Cheng, H. M. Ultrahigh-Voltage $LiCoO_2$ at 4.7 V by Interface Stabilization and Band Structure Modification. *Adv. Mater.* **2023**, 35 (22), No. 2212059, DOI: 10.1002/adma.202212059.
- (30) Huang, W.; Li, J.; Zhao, Q.; Li, S.; Ge, M.; Fang, J.; Chen, Z.; Yu, L.; Huang, X.; Zhao, W.; Huang, X.; Ren, G.; Zhang, N.; He, L.; Wen, J.; Yang, W.; Zhang, M.; Liu, T.; Amine, K.; Pan, F. Mechanochemically Robust LiCoO₂ with Ultrahigh Capacity and Prolonged Cyclability. *Adv. Mater.* **2024**, No. 2405519.
- (31) Li, S.; Zhang, W.; Wu, Q.; Fan, L.; Wang, X.; Wang, X.; Shen, Z.; He, Y.; Lu, Y. Synergistic dual-additive electrolyte enables practical

- lithium-metal batteries. Angew. Chem., Int. Ed. 2020, 59 (35), 14935–14941.
- (32) Zhang, J.; Wang, P.-F.; Bai, P.; Wan, H.; Liu, S.; Hou, S.; Pu, X.; Xia, J.; Zhang, W.; Wang, Z.; Nan, B.; Zhang, X.; Xu, J.; Wang, C. Interfacial design for a 4.6 V high-voltage single-crystalline LiCoO₂ cathode. *Adv. Mater.* **2022**, 34 (8), No. 2108353.
- (33) Zhang, X.; Zou, L.; Xu, Y.; Cao, X.; Engelhard, M. H.; Matthews, B. E.; Zhong, L.; Wu, H.; Jia, H.; Ren, X.; Gao, P.; Chen, Z.; Qin, Y.; Kompella, C.; Arey, B. W.; Li, J.; Wang, D.; Wang, C.; Zhang, J.-G.; Xu, W. Advanced Electrolytes for Fast-Charging High-Voltage Lithium-Ion Batteries in Wide-Temperature Range. *Adv. Energy Mater.* **2020**, *10* (22), No. 2000368.
- (34) Tan, X.; Zhao, T.; Song, L.; Mao, D.; Zhang, Y.; Fan, Z.; Wang, H.; Chu, W. Simultaneous Near-Surface Trace Doping and Surface Modifications by Gas—Solid Reactions during One-Pot Synthesis Enable Stable High-Voltage Performance of LiCoO₂. *Adv. Energy Mater.* **2022**, *12* (30), No. 2200008, DOI: 10.1002/aenm.202200008.
- (35) Abbaspour-Tamijani, A.; Bennett, J. W.; Jones, D. T.; Cartagena-Gonzalez, N.; Jones, Z. R.; Laudadio, E. D.; Hamers, R. J.; Santana, J. A.; Mason, S. E. DFT and thermodynamics calculations of surface cation release in LiCoO₂. *Appl. Surf. Sci.* **2020**, *515*, No. 145865, DOI: 10.1016/j.apsusc.2020.145865.
- (36) Cao, X.; Ahmad, N.; Zeng, C.; Pei, H.; Hua, Z.; Shao, R.; Zhang, L.; Yang, W. Zirconization of LiCoO₂ for enhanced stability and oxygen deactivation in all-solid-state lithium battery cathodes. *J. Energy Chem.* **2025**, *106*, 930–938.
- (37) Baddour-Hadjean, R.; Pereira-Ramos, J.-P. Raman microspectrometry applied to the study of electrode materials for lithium batteries. *Chem. Rev.* **2010**, *110* (3), 1278–1319.
- (38) Huang, H.; Li, Z.; Gu, S.; Bian, J.; Li, Y.; Chen, J.; Liao, K.; Gan, Q.; Wang, Y.; Wu, S.; Wang, Z.; Luo, W.; Hao, R.; Wang, Z.; Wang, G.; Lu, Z. Dextran sulfate lithium as versatile binder to stabilize high-voltage $LiCoO_2$ to 4.6 V. Adv. Energy Mater. **2021**, 11 (44), No. 2101864.
- (39) Li, X.; Qiao, Y.; Guo, S.; Jiang, K.; Ishida, M.; Zhou, H. A new type of Li-rich rock-salt oxide Li₂Ni_{1/3}Ru_{2/3}O₃ with reversible anionic redox chemistry. *Adv. Mater.* **2019**, *31* (11), No. 1807825.
- (40) Qiu, B.; Zhang, M.; Wu, L.; Wang, J.; Xia, Y.; Qian, D.; Liu, H.; Hy, S.; Chen, Y.; An, K.; Zhu, Y.; Liu, Z.; Meng, Y. S. Gas-solid interfacial modification of oxygen activity in layered oxide cathodes for lithium-ion batteries. *Nat. Commun.* **2016**, *7* (12), No. 12108.
- (41) Csernica, P. M.; Kalirai, S. S.; Gent, W. E.; Lim, K.; Yu, Y.-S.; Liu, Y.; Ahn, S.-J.; Kaeli, E.; Xu, X.; Stone, K. H.; Marshall, A. F.; Sinclair, R.; Shapiro, D. A.; Toney, M. F.; Chueh, W. C. Persistent and partially mobile oxygen vacancies in Li-rich layered oxides. *Nat. Energy* **2021**, *6* (6), 642–652.
- (42) Lyu, Y.; Wu, X.; Wang, K.; Feng, Z.; Cheng, T.; Liu, Y.; Wang, M.; Chen, R.; Xu, L.; Zhou, J.; Lu, Y.; Guo, B. An overview on the advances of LiCoO₂ cathodes for Lithium-Ion batteries. *Adv. Energy Mater.* **2021**, *11* (2), No. 2000982.
- (43) Zhang, J.-N.; Li, Q.; Ouyang, C.; Yu, X.; Ge, M.; Huang, X.; Hu, E.; Ma, C.; Li, S.; Xiao, R.; Yang, W.; Chu, Y.; Liu, Y.; Yu, H.; Yang, X.-Q.; Huang, X.; Chen, L.; Li, H. Trace doping of multiple elements enables stable battery cycling of LiCoO₂ at 4.6 V. *Nat. Energy* **2019**, *4* (7), 594–603.
- (44) Grimme, S.; Antony, J.; Ehrlich, S.; Krieg, H. A consistent and accurate ab initio parametrization of density functional dispersion correction (DFT-D) for the 94 elements H-Pu. *J. Chem. Phys.* **2010**, 132 (15), No. 154104.
- (45) Kresse, G.; Furthmüller, J. Efficiency of ab-initio total energy calculations for metals and semiconductors using a plane-wave basis set. *Comput. Mater. Sci.* **1996**, *6* (1), 15–50.
- (46) Grimme, S. Semiempirical GGA-type density functional constructed with a long-range dispersion correction. *J. Comput. Chem.* **2006**, 27 (15), 1787–1799.
- (47) Mattsson, A. E.; Armiento, R.; Schultz, P. A.; Mattsson, T. R. Nonequivalence of the generalized gradient approximations PBE and PW91. *Phys. Rev. B* **2006**, 73 (19), No. 195123, DOI: 10.1103/PhysRevB.73.195123.